ADVANCED MATERIALS
www.advmat.de

Dual-Cascade Responsive Nanoparticles Enhance Pancreatic Cancer Therapy by Eliminating Tumor-Resident Intracellular Bacteria

*Xiaoxu Kang, Fanqiang Bu, Wenli Feng, Fang Liu, Xuankun Yang, Haofei Li, Yingjie Yu, Guofeng Li, Haihua Xiao, and Xing Wang**

The limited drug penetration and robust bacteria-mediated drug inactivation in pancreatic cancer result in the failure of chemotherapy. To fight against these issues, a dual-cascade responsive nanoparticle (sNP@G/IR) that can sequentially trigger deep penetration, killing of intratumor bacteria, and controlled release of chemo-drug, is reported. sNP@G/IR consists of a hyaluronic acid (HA) shell and glutathione (GSH)-responsive polymer-core (NP@G/IR), that encapsulates gemcitabine (Gem) and photothermal agent (IR1048). The polymer core, as an antibiotic alternative, is tailored to exert optimal antibacterial activity and selectivity. sNP@G/IR actively homes in on the tumor due to the CD44 targeting of the HA shell, which is subsequently degraded by the hyaluronidase in the extracellular matrix. The resultant NP@G/IR in decreased size and reversed charge facilitates deep tumor penetration. After cellular endocytosis, the exposed guanidine on NP@G/IR kills intracellular bacteria through disrupting cell membranes. Intracellular GSH further triggers the controlled release of the cargo. Thus, the protected Gem eventually induces cell apoptosis. Under laser irradiation, the hyperthermia of IR1048 helps further elimination of tumors and bacteria. Moreover, sNP@G/IR activates immune response, thereby reinforcing anticancer capacity. Therefore, this dual-cascade responsive sNP@G/IR eliminates tumor-resident intracellular bacteria and augments drug delivery efficacy, providing a new avenue for improving cancer therapy.

1. Introduction

Pancreatic cancer is a highly fatal malignancy with a 5-year survival rate that remains under 10% after decades of efforts.[1] The main drawbacks of current pancreatic cancer chemotherapy include: i) numerous tumor biological barriers prevent drug penetration and efficient cellular internalization, leading to poor delivery efficiency;[2] and ii) various inactivation processes of drugs result in chemotherapeutic inefficiency and resistance.[3] Therefore, it is essential to develop a novel antitumor strategy that can not only augment drug transportation/penetration but also prevent drug inactivation to improve the treatment of pancreatic cancer.

To overcome tumor biological barriers, numerous engineered nanoparticles (NPs) have been developed.[4] The use of responsive nano-delivery-systems, which can modulate their physical properties (e.g., undergo size changes and charge reversal) in response to exogenous stimuli (e.g., light, irradiation) or endogenous stimuli (e.g., enzymes, pH, redox state), is considered an ideal strategy for deep tumor penetration.[5] However, inaccurate and uncontrolled release of a drug usually results in poor treatment efficacy.[4,6] As such, it is highly desirable to develop a cascade-responsive nano-delivery-system that can sequentially enhance tumor penetration and precisely control intracellular drug release to improve delivery efficiency.

Drug inactivation is another key parameter that determines the fate of a certain therapy.[7] Tumor-resident bacteria were reported to be responsible for drug inactivation. Bacterial enzymes can metabolize drugs to inactive forms, finally resulting in drug resistance.[8] Notably, the bacteria are present in the tumors of most patients with pancreatic cancer.[8,9] To prevent drug inactivation especially by bacteria, delivery of anticancer drugs accompanied by a certain antibiotic can help kill bacteria and thereby overcome bacteria-induced drug resistance.[10] While the simultaneous release strategy cannot completely block the degradation of drugs by bacteria due to hysteresis of the antibiotic bactericidal process. Furthermore,

X. Kang, F. Bu, W. Feng, X. Yang, H. Li, Y. Yu, G. Li, X. Wang
State Key Laboratory of Organic-Inorganic Composites
Beijing Laboratory of Biomedical Materials
Beijing University of Chemical Technology
Beijing 100029, P. R. China
E-mail: wangxing@mail.buct.edu.cn
F. Liu
Department of Oncology of Integrative Chinese and Western Medicine
China-Japan Friendship Hospital
Beijing 100029, P. R. China
H. Xiao
Beijing National Laboratory for Molecular Sciences
State Key Laboratory of Polymer Physics and Chemistry
Institute of Chemistry
Chinese Academy of Sciences
Beijing 100190, P. R. China
The ORCID identification number(s) for the author(s) of this article can be found under https://doi.org/10.1002/adma.202206765.

DOI: 10.1002/adma.202206765

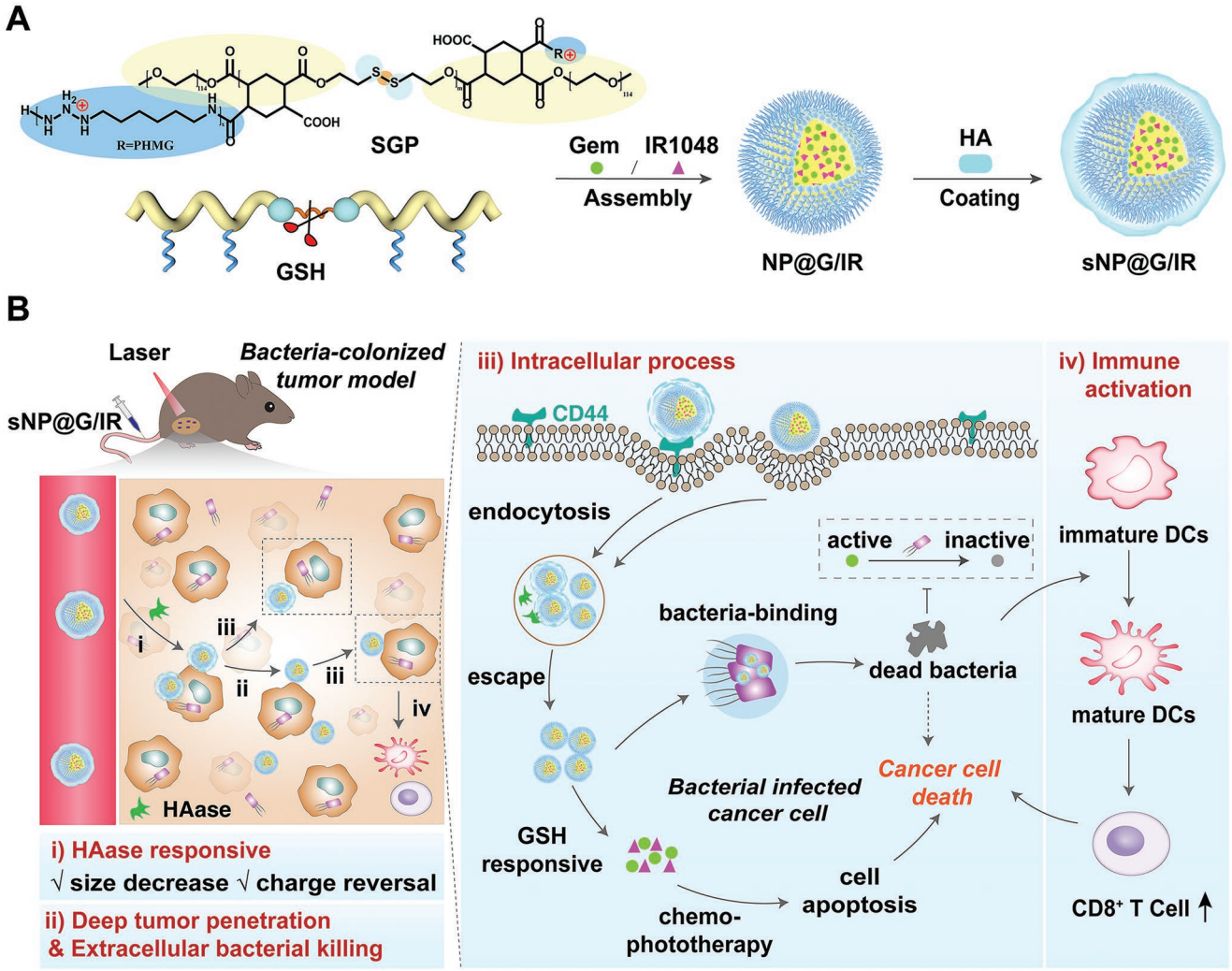

Scheme 1. A) Preparation process of the dual-cascade responsive sNP@G/IR with core–shell structure. B) sNP@G/IR suppresses bacteria-colonized tumor growth by eliminating tumor-resident intracellular bacteria and precise drug delivery. The process is divided into 4 steps: i) HAase in ECM promotes shell detachment and exposure of core nanoparticles (NP@G/IR); ii) the bare NP@G/IR with decreased particle size and reversed charge achieves deep tumor penetration and extracellular bacterial killing; iii) after rapid endocytosis, NP@G/IR facilitates the elimination of intracellular bacteria and the controlled release of drugs; iv) and immune activation by triggering $CD8^+$ T cells production.

recent studies highlighted that intratumoral bacteria are mostly intracellular.[11] The membrane barrier and harsh environment of host cells could also decrease intracellular accumulations of antibiotics and impair their efficacy.[12] Besides, long-term use of antibiotics is prone to inducing bacterial resistance.[13] As an alternative therapy, antibacterial polymers have shown the ability to overcome antibiotic resistance and treat recurring infections by a fast disruption of membrane.[14] Thus, using an antibacterial polymer to deliver anticancer drugs, enabling rapid bactericidal action before drug release, could offer an optimal option to overcome bacteria-mediated drug inactivation.

Gemcitabine (Gem), a cytidine nucleoside analog and the gold standard treatment drug for pancreatic cancer in clinics,[5e] is exactly such a drug that has difficulty in penetrating the dense tumor tissues and can be metabolized by bacteria in tumors.[9] Herein, we proposed a dual-cascade responsive NP with a so-called "offensive-defensive" maneuver to enhance pancreatic cancer therapy (**Scheme 1**), which can eliminate tumor-resident intracellular bacteria and realize precise drug delivery. An amphiphilic GSH-responsive polymer (SGP) with optimal antibacterial activity and selectivity was first used to load Gem and IR1048 to form a core NP (NP@G/IR, as shown in Scheme 1A). It was further coated with an enzyme-responsive hyaluronic acid (HA) to obtain the dual-cascade responsive NP (sNP@G/IR). With this subtle assembly (Scheme 1B): i) sNP@G/IR preferentially accumulated in the tumor site due to CD44 targeting of the HA shell, which could be subsequently degraded by hyaluronidase (HAase) in the extracellular matrix (ECM). ii) The released NP@G/IR in a decreased size and reversed charge facilitated deep tumor penetration. In this process, NP@G/IR killed encountered bacteria. Then, iii) positively charged NP@G/IR rapidly entered tumor cells. Their guanidine groups further killed the intracellular bacteria by disrupting the bacterial membrane. Besides, intracellular GSH triggered disulfides

breaking for controlled release of Gem and IR1048. Gem could thus be protected maximally from bacterial metabolism and successfully kill cancer cells. Moreover, the topical hyperthermia generated by IR1048 under laser irradiation improved the anticancer effect and bacterial elimination. Thereafter, iv) this treatment also modulated the innate immune responses of tumors by promoting the production of cytotoxic T cells, so as to reinforce the anticancer effect. In this way, bacteria in the tumor were eliminated and the Gem was protected synergistically, performing the exciting "offensive-defensive" maneuver. Therefore, the intelligent sNP@G/IR could greatly improve the therapeutic effect on pancreatic cancer.

2. Results and Discussions

2.1. Synthesis and Characterization of Polymers

The synthesis route of SGP is shown in Scheme S1, Supporting Information. First, a disulfide containing polymer, (poly(CHTA-*co*-HD)-PEG) (donated as SP), with pair-wised pendant carboxyl groups was synthesized.[15] According to the ^{1}H NMR and GPC, the molecular weight (M_w) of SP was ≈18 000 g mol^{-1} (Figures S1 and S2, Supporting Information). Polyhexamethyleneguanidine hydrochloride (PHMG), a commercially available guanidine-based antibacterial agent,[16] was introduced to the SP chain to synthesize SGP by an amide condensation reaction. PHMG endows SGP with high efficiency and long-term bactericidal properties.[17] However, we found that the increased amount of PHMG would result in high cytotoxicity. To balance the antibacterial activity and biocompatibility, a series of SGPs with different ratios of SP and PHMG (2:1, 5:1, and 10:1) were prepared, denoting as SGP_1, SGP_2, and SGP_3, respectively. ^{1}H NMR results showed that the grafted PHMG units in SGP_1, SGP_2, and SGP_3 were calculated to be 13, 7, and 4, respectively (Figure S3 and Table S1, Supporting Information). Such a modulation offered an opportunity to balance the antibacterial activity and selectivity of SGPs.

The antibacterial activity of SGPs was determined through the minimum inhibitory concentration (MIC) against the model bacterium, *Escherichia coli* Nissle 1917 (EcN). EcN has been reported to metabolize Gem to an inactive form.[9] SGPs displayed PHMG-ratio dependent activity against EcN. SGP_1 and SGP_2 showed better antibacterial activity with MICs of 62.5 and 250 μg mL^{-1}, respectively, while the MIC of SGP_3 was found over 250 μg mL^{-1}. To investigate the membrane-disrupting toxicity of SGPs on mammalian cells, their ability to lyse red blood cells was examined.[18] The hemolysis of SGPs was determined by HC_{10}, that is, the concentration of polymers to cause 10% hemolysis. The HC_{10} of SGPs were 156, 5000, and >5000 μg mL^{-1}, in the above sequence. It showed the increased PHMG units of SGPs enhanced the lysis of RBCs. The selectivity index (SI) was further calculated by HC_{10}/MIC, which could indicate the cell-type selectivity of polymers.[14c,19] Among them, SGP_2 exhibited the best SI value of 20 (Table S1, Supporting Information), suggesting SGP_2 was an ideal vehicle to balance antibacterial activity and selectivity. To further confirm this, the cytotoxicity of SGP_2 on mammalian cells, including mouse epithelioid fibroblasts L929 cells and mouse pancreatic cancer cells Pan02, was examined by methyl thiazolyl tetrazolium (MTT) assay (Figure S4, Supporting Information). The cell viabilities of these two cell lines were both above 80% when SGP_2 at 250 μg mL^{-1} (1 × MIC), indicating SGP_2 has good biocompatibility and was suitable to use as a drug vehicle.[20]

2.2. Assembly and Characterizations of NPs

To prepare NPs, SGP_2 was used to load either Gem or IR1048, as well as to co-load both Gem and IR1048 (Table S2, Supporting Information). The obtained NPs were called NP@G, NP@IR, and NP@G/IR, respectively. As a control, SGP_2 was allowed to self-assemble into blank NPs without Gem and IR1048 (denoted as NP_0). The highest drug loading content (DLC) of Gem and IR 1048 in NP@G/IR reached 19.9% and 9.7%, respectively (Table S3, Supporting Information). Subsequently, HA was coated on the above mentioned NPs to form the final NPs, that is, sNP@G, sNP@IR, sNP@G/IR, and sNP_0 (Table S2, Supporting Information). The spherical morphologies of NP@G/IR and sNP@G/IR with uniform sizes were observed by TEM (**Figure 1**A,B). sNP@G/IR exhibited a distinct core–shell structure. The DLS results demonstrated that the size of NP@G/IR increased from 64.1 to 152.3 nm after HA coating (sNP@G/IR), while the zeta potential decreased from +11.7 to −13.0 mV (Figure S5, Supporting Information). In the presence of HAase, the HA shell in sNP@G/IR was degraded to expose NP@G/IR (Figure 1C), resulting in a size decrease to 73.0 nm, and a zeta potential shift to +0.1 mV (Figure 1D,E). Afterward, the size stability of NP@G/IR and sNP@G/IR was tested in various culture media (Figure S6, Supporting Information). NP@G/IR and sNP@G/IR maintained relatively uniform hydrodynamic sizes in PBS, water, 10% FBS, and LB medium for 5 days, suggesting that they were stable and suitable for anticancer or antibacterial applications.

GSH can trigger the breakage of disulfide bonds in SGP.[21] In order to test the GSH-responsive behavior of SGP_2, a validated assay via a 1,2-benzenedicarboxaldehyde (OPA) derivative was performed by monitoring the breakage of the disulfide units in the polymer chain (Scheme S2, Supporting Information).[22] The half-lives of GSH incubated with 2-hydroxyethyl disulfide and SGP_2 were 3.0 h and 1.7 h, respectively (Figure S7A–D, Supporting Information). Furthermore, the GSH-responsiveness of SGP_2 was confirmed by GPC. After incubation with 10 × 10^{-3} M GSH for 24 h, the M_w of SGP_2 decreased from 23 099 to 6295 g mol^{-1}. This implied that SGP has been degraded to methoxyl-polyethylene glycol ($mPEG_{5K}$) and other small fragments (Figure S7E, Supporting Information).

sNP@G/IR is responsive to both HAase and GSH. To demonstrate whether its dual responsiveness is in a cascade manner, we explored the particle size and polydispersity index (PDI) changes of sNP@G/IR in the mimicked tumor microenvironment (Figure 1F and Figure S8, Supporting Information). In the HAase-free environment, sNP@G/IR was stable even in the presence of GSH. In contrast, HAase incubation could lead to a size decrease of ≈60 nm in sNP@G/IR at 4 h. Prolonging incubation time, the obtained NP@G/IR was stable. But in the presence of GSH, NP@G/IR would collapse completely owing

to the exposure and breakage of disulfide bonds, thus resulting in a cascade-responsiveness on HAase-GSH.

Gem release profiles were evaluated in different solutions (Figure 1G,H). At pH 7.4, pH 5.0, and 10×10^{-3} M of GSH, the release rates of Gem from sNP@G/IR were 26.34%, 29.90%, and 34.55% after 48 h respectively. After detaching the HA shell of sNP@G/IR by the addition of HAase, the percentage of Gem released from NP@G/IR did not show notable changes at pH 7.4. In contrast, Gem was released very rapidly at pH 5.0 or in the presence of GSH, which was up to 66.66% and 93.75%, respectively. Accordingly, we can infer that sNP@G/IR may have better performance in blood circulation while avoiding the immature leakage of anticancer drugs with a high chance of successfully delivering anticancer drugs to tumor sites and cellular loci.

The photothermal properties of sNP@G/IR were then examined. Because of the loaded IR1048, the NPs showed an absorption peak at 1051 nm in the UV spectra (Figure S9A, Supporting Information).[23] After irradiating with 1064 nm light at 1.0 W cm^{-2} for 10 min, the solution temperature of sNP@G/IR increased by 15.4 and 41.8 °C at 2.5 and 40 μg mL^{-1} of IR1048 respectively (Figure 1I, and Figure S9B, Supporting Information). Moreover, sNP@G/IR exhibited good photothermal stability, and the thermal effect of the sNP@G/IR solution did not diminish after four times of laser on/off cycles (Figure S9C, Supporting Information). These studies confirmed the good photothermal therapeutic ability of sNP@G/IR.

2.3. In Vitro Antibacterial Activity

To verify the antibacterial activity of sNP@IR, various formulations (i.e., PBS, NP_0, sNP_0, NP@IR, sNP@IR) were inoculated with EcN suspensions in LB medium, and the OD600 was measured at specific times. After sNP_0 treatment, the starting point of exponential growth period was postponed from 4 h to 12 h, while in the sNP@IR+L group, the replication of bacteria was completely inhibited within 24 h (**Figure 2**A). Furthermore, the quantitative antibacterial efficiency was evaluated by a colony count method. There was a 3-$\log_{10}$ CFU reduction in

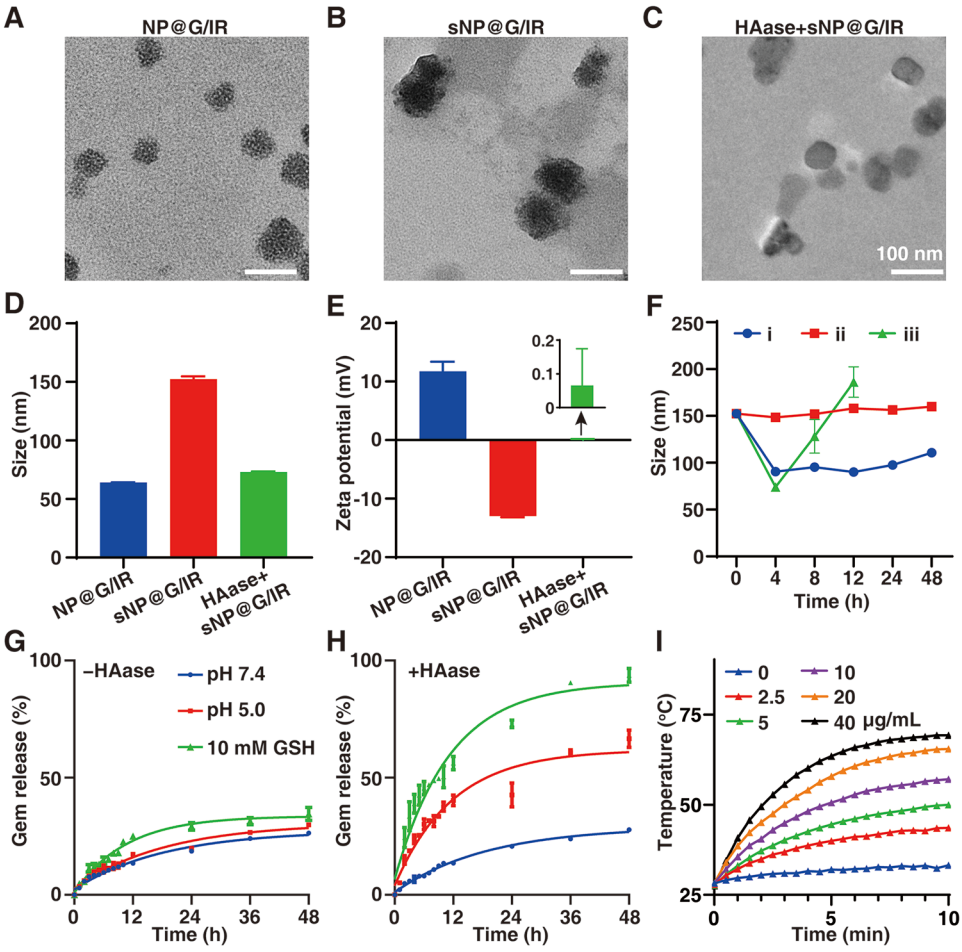

Figure 1. In vitro characterizations of sNP@G/IR. A–C) TEM images of NP@G/IR (A), sNP@G/IR (B), and sNP@G/IR (C) incubated with HAase (110 IU mL^{-1}). D) Particle size and E) zeta potential of NP@G/IR, sNP@G/IR, and sNP@G/IR incubated with HAase, $n = 3$. F) Particle size variation of sNP@G/IR in various buffer solutions at pH 6.5: i) HAase; ii) 10×10^{-3} M GSH; iii) HAase and 10×10^{-3} M GSH, $n = 3$. G,H) Gem release profiles of sNP@G/IR in different conditions: G) without HAase and H) with HAase, $n = 3$. I) Temperature-variation curves of sNP@G/IR solutions in water at various IR1048 concentrations after irradiation by a 1064 nm laser at 1.0 W cm^{-2} for 10 min.

the number of bacterial colonies after being treated with sNP_0 for 8 h, and bacteria treated with sNP@IR+L were all killed (Figure 2B,C). These results suggested that guanidine conferred good antibacterial activity of sNP@IR, and the photothermal effect triggered by IR1048 laser irradiation provided a powerful boost for complete bacterial eradication.

Furthermore, the antibacterial activity of sNP@IR was visualized using a LIVE/DEAD Bacterial Viability Kit by confocal laser scanning microscopy (CLSM) (Figure S10, Supporting Information). Most of the bacteria exhibited green fluorescence (FL) (live) when treated with PBS, and an increased red FL (dead) was found in the bacteria treated with sNP_0. Following sNP@G/IR treatment upon laser irradiation, almost all bacteria exhibited red FL (dead), which was consistent with the results of the growth curves and colony counts.

To figure out the intrinsic mechanism, the interaction between NP_0 and EcN was explored. SGP_2 loaded with Rhodamine B (RhB) assembled into NPs (denoted as NP@RhB) in DMSO/water. As shown in Figure 2D, NP@RhB exhibited red FL and was mostly co-located with the green EcN. The FL intensity profiles showed a high overlap of red and green FL, indicating that NP@RhB could actively bind to the bacteria (Figure 2E). Further, 3,3′-dipropylthiadicarbocyanine iodide ($DiSC_35$) dye, which can probe changes in plasma membrane potential, was applied to evaluate the bacterial plasma membrane depolarization ability of the NP_0.[24] The FL intensity of EcN obviously increased after treating with NP_0 for 30 min, and the increase was positively correlated with the concentration of NP_0 (Figure 2F). These results suggested that NP_0 would depolarize the membrane after binding the bacterial membrane. Subsequently, we observed the morphology of bacteria with different treatments (Figure 2G). SEM images showed that the bacteria in the control PBS groups were normal in shape and maintained clear borders as well as membrane integrity. However, there was a severe collapse of the bacterial cell membrane. The cell wall fragmentation and irregularly shaped pores could be seen clearly in the bacteria treated with various NPs. These suggested that sNP@IR exerted antibacterial properties by disrupting bacterial cell membranes and cell walls, which were conferred by guanidine groups and photothermal effect.[17b,25]

2.4. In Vitro Intracellular Anticancer Activity and Antibacterial Activity

In order to explore the intracellular mechanism of sNP@G/IR, CLSM and flow cytometry were performed respectively to visualize and quantify the cellular uptake of sNP@G/IR.[27] First, both NP_0 and sNP_0 encapsulating RhB were prepared and denoted as NP@RhB and sNP@RhB, respectively. As the co-incubation time of Pan02 cells increased, the intracellular red FL intensity increased quickly in the sNP@RhB group, suggesting rapid internalization of sNP@RhB (Figure S11, Supporting Information). Meanwhile, in the NP@RhB group, the similar phenomena could be seen (**Figure 3**A). Quantitative analysis by flow cytometry further confirmed above uptake behaviors (Figure 3B, and Figure S12, Supporting Information), although these two NPs had different surface functional groups.

Since sNP@RhB was designed with HA shell to shield positive charge of NP@RhB while assembling targeted HA molecules on its surface, the endocytosis pathway of sNP@RhB should be precise recognition of HA pendants, rather than the general charge interaction between NP@RhB and cells.[26] To validate the recognition process, a competitive inhibition assay was performed (Figure 3A,B, and Figure S12, Supporting Information). Free HA molecules were employed here for the pre-incubation for 2 h. After that, both sNP@RhB and NP@RhB were added to the cultures. Significantly, the red FL intensity in sNP@RhB-treated cells was sharply decreased (****, $p = 0.0000008$), while that in NP@RhB-treated cells was still strong. Depending on literatures report,[27] the cellular uptake of sNP@RhB should be a CD44 receptor-mediated endocytosis pathway. Thus, HA coating upgraded the common electrostatic interaction between guanidine groups on NP@RhB and cell membranes that could lead to a rapid internalization of most NPs.

Subsequently, the lysosomal escape behavior of sNP@RhB was examined. sNP_0 was first labeled with fluorescein isothiocyanate (FITC) that was denoted as sNP@FITC (green). The lysosomes of Pan02 cells were stained in red FL by a LysoTracker Red dye. After 3 h co-incubation of sNP@FITC, the green and red FL in Pan02 cells mostly overlapped (Figure 3C, Figure S13A, Supporting Information). After refreshing the culture medium (to remove NPs) and culturing additional 1 h and 3 h, overlap of the green and red FL decreased with time prolonging. The co-localization ratio between sNP@FITC and lysosomes was calculated beyond 66% before refreshing the medium (Figure 3D, Figure S13B, Supporting Information), while decreased to lower than 30% after additional 3 h culture (***, $p = 0.0001$). In addition, when the cells were pre-treated with HA, the co-localization ratio was only 49% at the beginning and decreased to lower than 18% according to the above test points (****, $p = 0.0000007$). These phenomena not only demonstrated the specific targeting action, but also revalidated the lysosomal escape of sNP. This behavior can be attributed to the degradation of the HA shell in lysosome, leading to guanidine exposure of the sNP and facilitating the transport of the resulting NP from lysosome to cytoplasm.[28] The above maneuvers were essential for exerting intracellular antibacterial and anticancer activities.

Next, cytotoxicity of sNP@G/IR was assessed by an MTT assay. Due to the combined potency of Gem and hyperthermia, more than 85% of cells were killed according to a relatively cell viability of 14.18% in sNP@G/IR+L group by loading 1 μg mL^{-1} Gem and 3.75 μg mL^{-1} IR1048 (Figure 3E). When sNP@G was used without laser irradiation, 52% of cells were killed due to the drug release of Gem; while when utilizing sNP@IR, most of the cells survived without laser treatment but only 60% of live cells were left under laser condition (Figure S14, Supporting Information). Obviously, Gem and hyperthermia contributed comparable amounts of cytotoxicity. In-depth analysis revealed that sNP@G/IR+L induced an apoptosis rate of 90.68% (Figure 3F, Figure S15, Supporting Information), while in the sequence of Gem, sNP@G, and sNP@IR+L, the rates were 23.29%, 38.75%, and 58.02%, respectively. This outcome was consistent with the results of cytotoxicity.

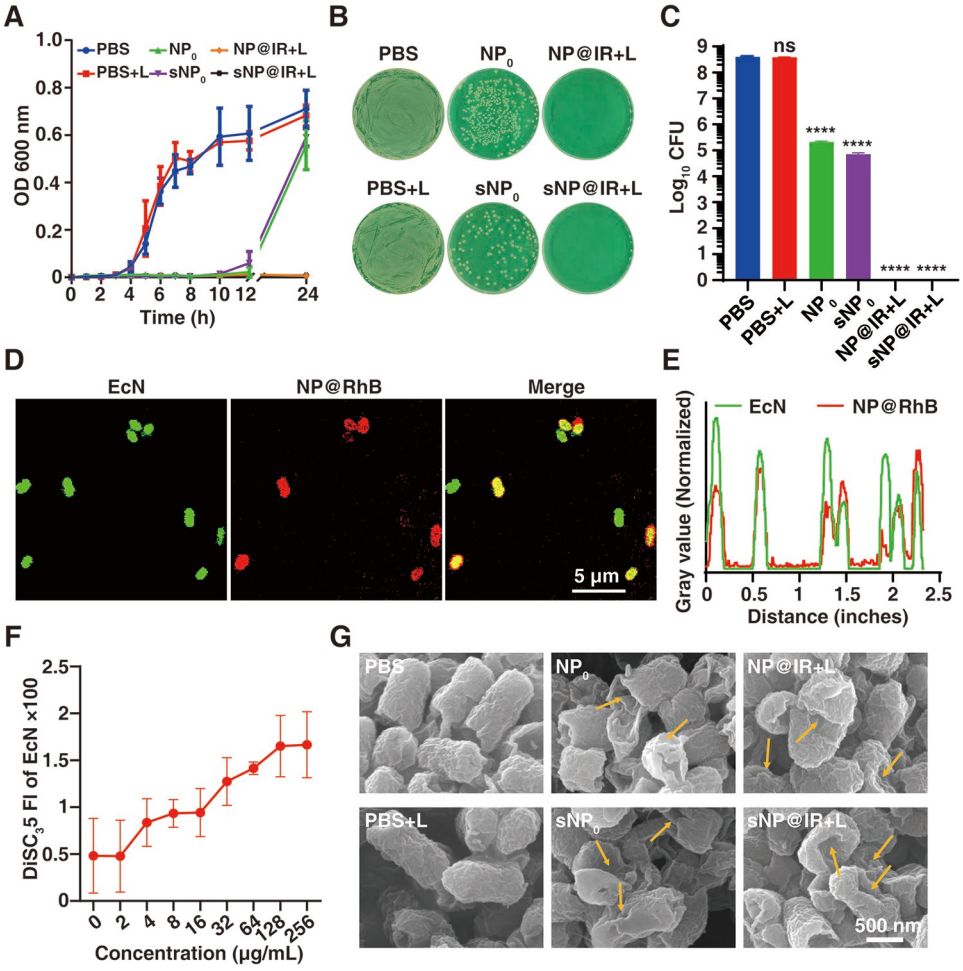

Figure 2. In vitro antibacterial activity of sNP@IR. A) Growth curves of EcN with various drugs. The concentrations of SGP_2 and IR1048 were set at 100 and 7 μg mL^{-1} respectively, $n = 3$. B) Colony plate images and C) the colony-forming units (CFUs) statistics of EcN treated with various drugs at 8 h in LB medium, $n = 3$. D) Confocal images of GFP-labeled EcN treated with NP@RhB for 30 min. E) Co-localization FL intensity profiles of GFP-labeled EcN and NP@RhB. F) The membrane depolarization of EcN treated with NP_0. G) SEM images of EcN treated with different drugs. The yellow arrows indicate the shape damage to bacterial cells. ****, $p < 0.0001$, ns, $p > 0.05$, respectively.

The bactericidal ability of sNP@IR against intracellular bacteria (EcN) was further tested based on abundant intracellular bacteria in tumors.[12] Pan02 cells infected with EcN (multiplicity of infection = 10, see Supporting Information for the details) were treated with various NPs and then were lysed by 0.1% Triton X-100 for CFUs counting (Figure 3G). For the employed sNP@IR, the concentrations of SGP_2 carrier and IR1048 were 256 and 17.9 μg mL^{-1}. Hence, the intracellular EcN was significantly suppressed when treated by sNP_0 for 24 h (5-$\log_{10}$ CFU reduction in Figure 3H, ****, $p = 0.00001$), which contributed to the excellent membrane penetration ability and efficient bactericidal activity. Besides, NP_0 displayed the same bactericidal activity due to similar cellular uptake (Figure 3A). After laser exposure, both NP@IR and sNP@IR could completely kill intracellular EcN (****, $p = 0.00001$), indicating the superior efficacy to eliminate intracellular bacteria by the combination of guanidine and photothermal treatment.

sNP@IR exhibited excellent ability to eliminate intracellular bacteria, which inspired us to evaluate the performance of sNP@G/IR to protect Gem when cocultured with bacteria. High-performance liquid chromatography (HPLC) was performed to determine the concentration of Gem under various conditions. The retention time of Gem in RPMI 1640 medium could be referred to at 8.492 min (Figure S16, Supporting Information, blue curve), but when cocultured with EcN, no intact Gem could be found, confirming the bacteria-mediated inactivation (Figure S16, Supporting Information, red curve). Excitingly, the conservation rate of Gem was found to be ≈83% in the coculture suspensions of sNP@G/IR and EcN after 1064 nm laser irradiating for 10 min at 1.0 W cm^{-2} (Figure S16, Supporting Information, green curve). This result suggested that Gem was successfully protected by sNP@G/IR from bacteria-mediated inactivation.

Furthermore, comprehensive assessment for killing cancer cells with infected bacteria was carried out. The bacteria-cell coculture system was achieved by adding bacterial suspensions to adherent Pan02 cells,[11] in which both extra- and intra-cellular bacteria existed. After treatments with the above NPs, the bacterial colonies were plated on LB agar, and the cell survival

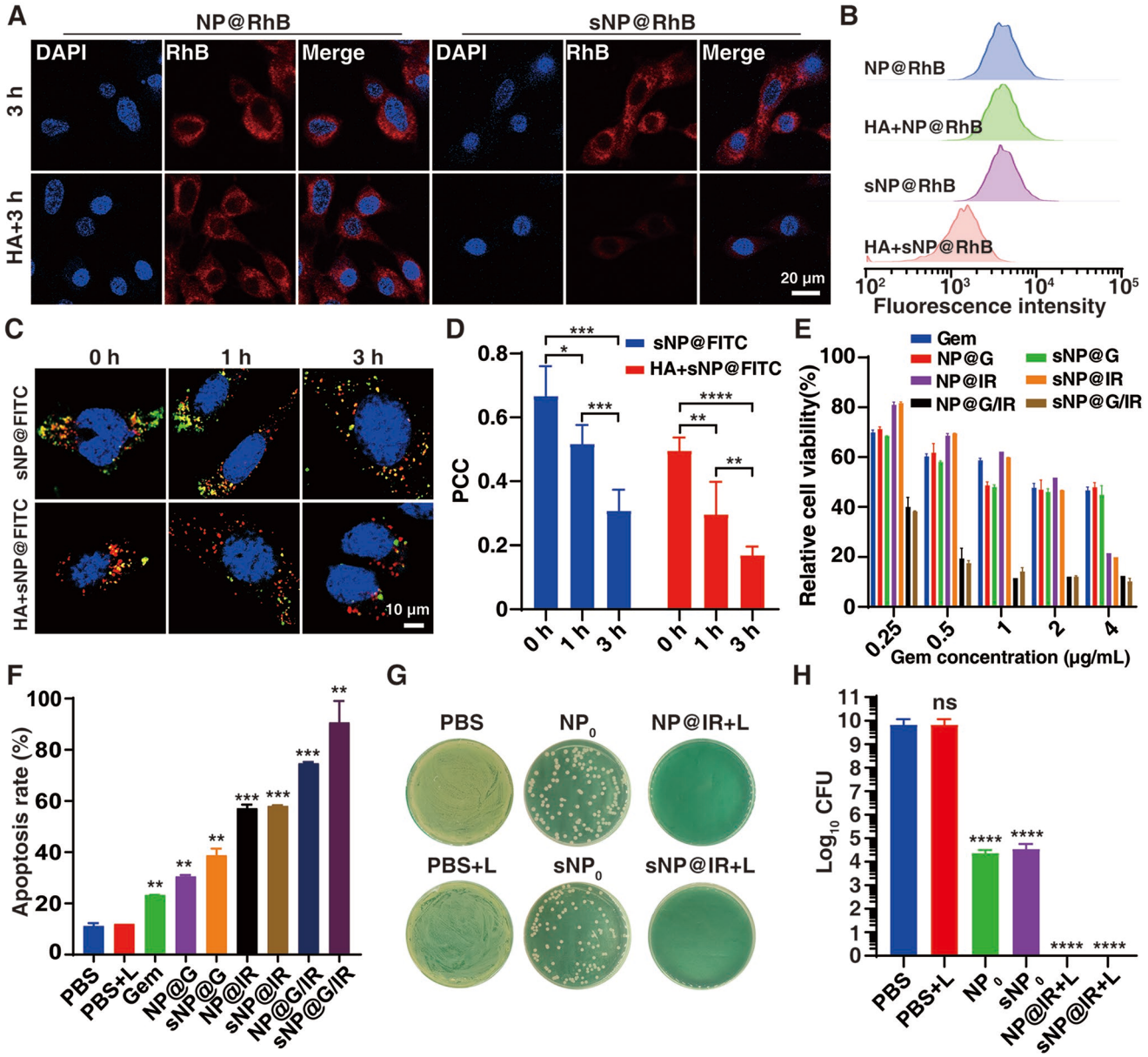

Figure 3. The intracellular behavior of sNP@G/IR in vitro. A) CLSM images and B) fluorescence profiles of Pan02 cells pretreated with or without HA and then incubated with NP@RhB and sNP@RhB for 3 h. C) CLSM images of the co-localization sNP@FITC and lysosomes in Pan02 cells pretreated with or without HA. After 3 h of incubation with sNP@FITC, the NPs were removed and the cells were incubated for an additional 1 h or 3 h for CLSM observation. Blue fluorescence comes from cell nucleus, red fluorescence comes from lysosomes, and green fluorescence comes from sNP@FITC, respectively. D) The corresponding overlap efficiency between sNP@FITC and lysosomes, which was analyzed by software Image J. Pearson's correlation coefficient is denoted as PCC, $n = 5$. E) Relative cell viability of Pan02 cells following various treatments, $n = 3$. F) Cell apoptosis rate of Pan02 cells treated with different formulations, as determined by flow cytometry, $n = 3$. G) Photos and H) CFUs of intracellular EcN with different treatments. The corresponding concentrations of SGP_2 and IR1048 were 256 and 17.9 μg mL^{-1}, respectively. **** $p < 0.0001$, *** $p < 0.001$, ** $p < 0.01$, and * $p < 0.05$, respectively.

rates were evaluated by a live/dead staining kit. To validate this model, free Gem herein did not perform any efficiency with a live cell ratio of 90.62%. When treated with sNP@G, a live cell ratio of 64.48% was recorded at the same concentration of Gem (Figure S17, Supporting Information), meanwhile resulting in 1.6-log_{10} CFU reduction of EcN (****, $p = 0.00001$, Figure S18, Supporting Information). After introducing photothermal treatment, sNP@G/IR killed EcN by 99.98% (3.7-log_{10} CFU reduction, ****, $p = 0.00001$), and Pan02 cells by 98.03% (red in live/dead confocal images). These results demonstrated the hypothesis that the proposed sNP@G/IR could exert the effectiveness of Gem by a sequential process of bactericidal and drug-release, and potentially would display superior therapeutic effects on cancer cells with commensal bacteria.

2.5. Evaluation of Deep Tumor Penetration, Targeting, and Photothermal Performances

In vitro 3D multicellular tumor spheroids (MTSs) mimicking Pan02 tumor tissues were adopted, to evaluate the penetration of sNP@G/IR. The strong FL in Pan02 MTSs incubated with sNP@RhB was observed in CLSM images at the cross-section of 32 µm (**Figure 4**A). Whereas, with the increase of depth from 32 to 48 µm, the FL gradually weakened. When the Pan02 MTSs were pre-treated with HAase for 2 h,[5c] a stronger FL intensity was detected (Figure 4A,B), even at 48 µm (Figure S19, Supporting Information). These results demonstrated that the HA shell degradation of sNP@RhB could enhance deep penetration because of the decreased particle size and increased zeta potential.

Subsequently, the in vivo biodistribution of sNP@G/IR was assessed in Pan02-tumor-bearing C57BL/6 mice by an in vivo imaging system (IVIS). Cy7.5 was adopted to label NP_0 and sNP_0 which were denoted as NP@Cy7.5 and sNP@Cy7.5, respectively. The following in vivo imaging showed the accumulation of NP@Cy7.5 and sNP@Cy7.5 in the tumor region increased gradually and peaked at 9 h after drug intravenous (i.v.) injection (Figure 4C,D). Clearly, the HA coating rapidly improved the accumulation just from 3 h. Tumors in the sNP@Cy7.5-treated mice had stronger FL intensity than those in the NP@Cy7.5 treatment group (*, $p < 0.05$), demonstrating the good targeting capability of sNP@Cy7.5. In addition, the distribution of FL in tumors and major organs at 9 h was tracked (Figure S20, Supporting Information). Quantitative FL

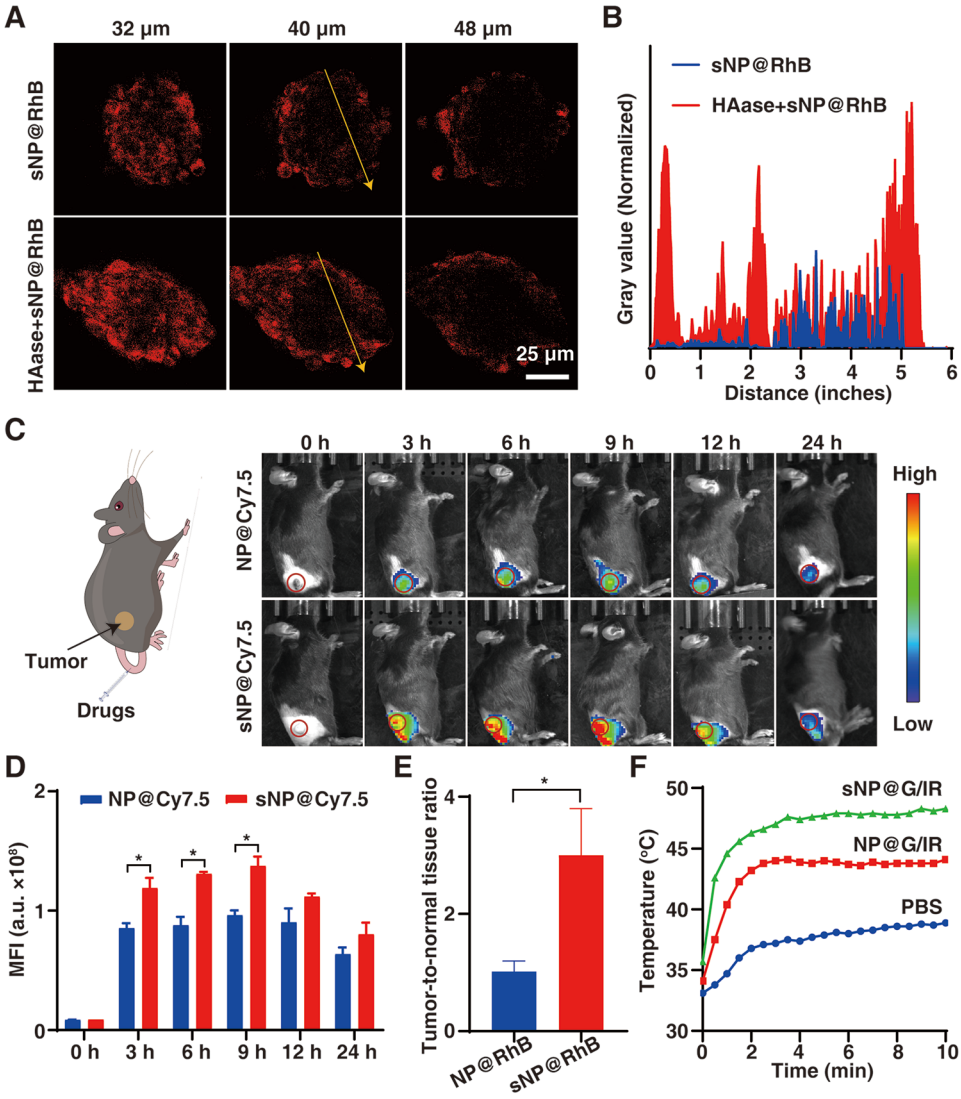

Figure 4. In vitro permeability as well as in vivo targeting ability and photothermal performance of sNP@G/IR. A) CLSM images of Pan02 MTSs treated with sNP@RhB and HAase + sNP@RhB for 3 h. B) The variance in fluorescence signal intensity along the yellow lines from the Pan02 MTSs. C) The tumor targeting study of NP@Cy7.5 and sNP@Cy7.5 in Pan02-tumor-bearing mice. D) The corresponding FL intensity of the tumor site at different time points, $n = 3$. E) Ex vivo analysis of tumor-to-normal tissues FL intensity ratio at 9 h after i.v. injection of NP@Cy7.5 and sNP@Cy7.5, $n = 3$. F) Temperature variation curves at the tumor sites of Pan02-tumor-bearing mice under 1064 nm laser irradiation with a power of 1.0 W cm^{-2} for 10 min (Gem, 10 mg kg^{-1}, IR1048, 3 mg kg^{-1}, i.v. injection). * $p < 0.05$.

intensity of tumor-to-normal tissues in the mice injected with sNP@Cy 7.5 was approximately three times that in the NP@Cy7.5 injected group (*, $p = 0.01$) (Figure 4E), proving a better tumor targeting and penetration of sNP@G/IR in vivo.

Furthermore, the photothermal performance in vivo of sNP@G/IR was examined (Figure 4F). Compared to the PBS-treated mice, an obvious temperature increase was recorded in the tumors of mice treated with NP@G/IR and sNP@G/IR, respectively. Notably, the temperature change in tumors of mice treated with sNP@G/IR (ΔT 12.6 °C) was also higher than that in the NP@G/IR treatment group (ΔT 10.0 °C), which agreed with the results from IVIS.

2.6. In Vivo Biosafety and Therapeutic Evaluation

To systematically investigate the biosafety profiles, healthy C57BL/6 mice ($n = 3$) were administered with PBS, sNP@G, sNP@IR, and sNP@G/IR by i.v. injection. The formulations were subjected to mice once every 2 for 14 days. The weight of the mice in the treatment groups showed no difference in comparison with that of mice in the PBS group (Figure S21A, Supporting Information). After 14 days, the blood and major organs (including heart, liver, spleen, lung, and kidney) of mice were collected. The serum biomarkers were all at normal levels compared to the control. Hematoxylin and eosin (H&E) staining of the major organs exhibited normal histomorphology with no obvious pathological abnormalities. Taken together, sNP@G, sNP@IR, and sNP@G/IR displayed acceptable biocompatibility (Figure S21B,C, Supporting Information).

The in vivo therapeutic efficacy of sNP@G/IR on bacteria-free Pan02-tumor-bearing mice was first evaluated. The mice were randomly grouped, including PBS, Gem, NP@G, sNP@G, NP@IR+L, sNP@IR+L, NP@G/IR+L, and sNP@G/IR+L, respectively. As shown in Figure S22A, Supporting Information, the mice were administered with these formulations on days 1, 4, and 7. At 9 h after injection, the tumors of mice in NP@IR+L, sNP@IR+L, NP@G/IR+L, and sNP@G/IR+L groups were irradiated with a 1064 nm laser under 1.0 W cm^{-2} for 10 min. Compared with free Gem (43.4% in tumor inhibition), sNP@G treatment exhibited 1.3 times antitumor activity (56.6% in tumor inhibition) due to a greater accumulation of sNP@G at the tumor site (Figure S22B–D, Supporting Information). Comparatively, sNP@G/IR+L treatment significantly suppressed tumors with a tumor inhibition rate of 98.7% (****, $p = 0.000001$), indicating the excellent combined therapeutic efficacy of chemotherapy and photothermal therapy (PTT). Compared with NP@G/IR+L group (93.9% in tumor inhibition), the average tumor weight in sNP@G/IR+L group was obviously decreased (**, $p = 0.006$), which was attributed to the tumor-targeted HA shell (Figure S22D, Supporting Information). In addition, the body weight of mice after different treatments showed no obvious difference (ns, $p > 0.05$) (Figure S22E, Supporting Information). Further H&E staining of the tumor sections displayed marked apoptosis as a consequence of chemotherapy and PTT triggered by sNP@G/IR+L treatment (Figure S22F, Supporting Information).

Encouraged by these results, we further assessed the capability of sNP@G/IR to suppress bacteria-colonized tumors. This tumor model was obtained by injecting EcN bacteria into tumor-bearing mice via i.v. injection.[9,29] To verify the successful establishment, FL intensity of tumors and major organs in mice was determined by IVIS after injecting GFP-labeled EcN at different time points. Tumors on days 1, 2, and 3 of bacterial injection all exhibited significantly enhanced FL intensity compared to the uninjected group (**, $p < 0.01$), indicating EcN colonization in the tumor site (Figure S23A,B, Supporting Information). Further, the long-term colonization ability of EcN in tumor site was investigated. On days 1, 2, 3, and 14, tumor tissues isolated from mice were homogenized and plated on LB agar. EcN was confirmed could be stably colonized in tumor tissue with ≈10^8 CFU g^{-1} (Figure S23C,D, Supporting Information), which is consistent with previous reports.[30] Based on these results and in-depth understanding,[11] intracellular bacteria in tumor cells were further quantified. Tumor cells were dissociated from tumor tissues, and extracellular bacteria were subsequently killed by staphylococcal lysozyme. A large amount of the bacteria in tumor tissue are intracellular bacteria (Figure S22E,F, Supporting Information).

Subsequently, the comprehensive therapeutic efficacy of sNP@G/IR+L against EcN colonized tumors was examined. The mice were randomly divided into 6 groups, including PBS, Gem, sNP@G, sNP@IR+L, NP@G/IR+L, and sNP@G/IR+L. Mice are treated according to the timeline (**Figure 5**A). Similarly, the following conditions, 1064 nm laser at 1.0 W cm^{-2} for 10 min, were used in the photothermal treatment groups. On the seventh day, after mice were treated twice with different formulations, tumors were extracted from the mice, homogenized, and plated on LB agar. Compared with Gem group (7.5-$\log_{10}$ CFU) that did not show activity (Figure 5B, Figure S24, Supporting Information), sNP@G effectively killed intratumor EcN (6.3-$\log_{10}$ CFU), with a 1.2-$\log_{10}$ CFU decrease owing to the bactericidal guanidine groups. After cooperation with PTT, CFU in the sNP@G/IR+L group (3.9-$\log_{10}$ CFU) was found significantly lower than that of sNP@G (6.3-$\log_{10}$ CFU, **, $p = 0.004$), sNP@IR+L (5.9-$\log_{10}$ CFU, *, $p = 0.02$) and NP@G/IR+L (5.2-$\log_{10}$ CFU, *, $p = 0.01$). sNP@G/IR+L displayed the best bacterial elimination effect. These results manifested that sNP@G/IR was expected to augment the total therapeutic efficacy.

After three times of treatments on days 1, 4, and 7 totally, the relative tumor volume (V/V_0) and body weight of mice were then monitored for 14 days. It could be seen that Gem had limited anticancer activity (the V/V_0 was 5.53) due to the bacteria-mediated drug inactivation (to PBS control, ns, $p > 0.05$, Figure 5C). In contrast, when treating with sNP@G, the V/V_0 was decreased to 2.05 (**, $p = 0.002$) indicating sNP@G improved the treatment effect on tumors by killing the intratumoral bacteria. Notably, the most suppressive ability against EcN-colonized tumors was shown in sNP@G/IR+L group (the $V/V_0 = 0.43$, ****, $p = 0.00001$), which was better than that of NP@G/IR+L group (the $V/V_0 = 1.20$, *, $p = 0.04$). Besides, within 14 days, the body weight of mice subjected to various formals showed no obvious differences (Figure S25, Supporting Information).

Furthermore, we examined the survival spans of mice in each treatment group within 60 days. In the groups of PBS, Gem, sNP@G, and sNP@IR+L, all mice died within 52 days. While the median survival time of mice treated with NP@G/IR+L was

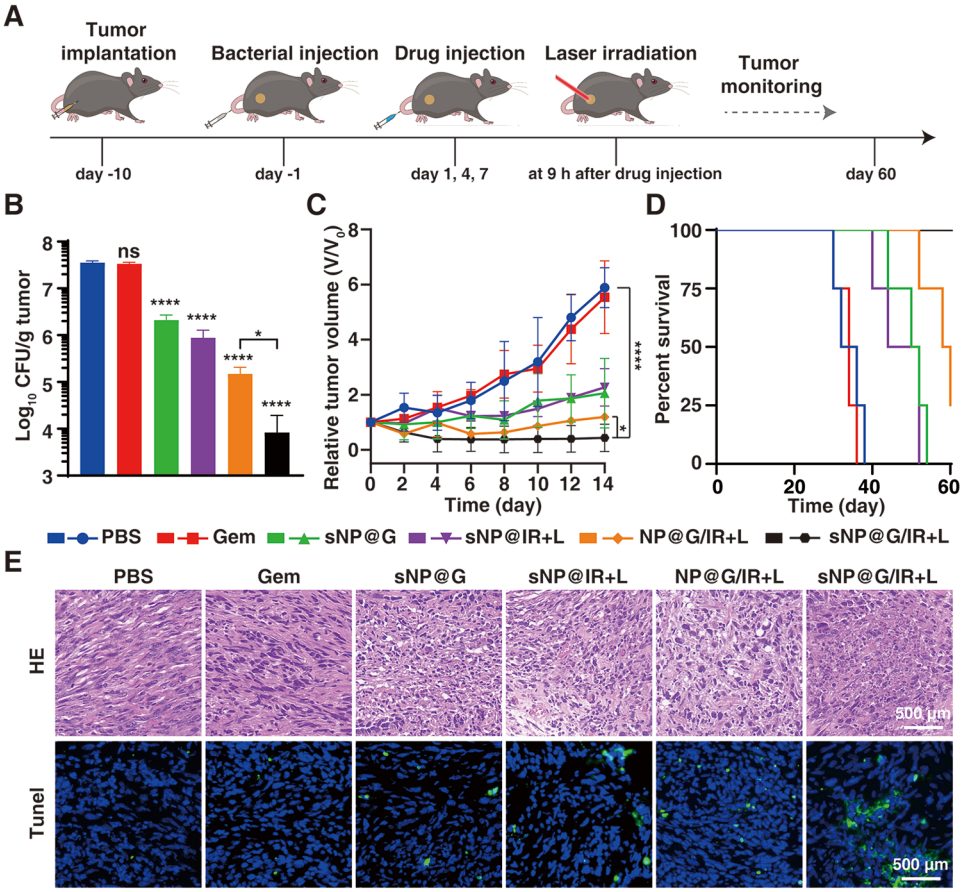

Figure 5. In vivo antitumor efficacy of sNP@G/IR on EcN-colonized subcutaneous Pan02 tumor model. A) Timeline of in vivo treatment. B) CFU in tumors of mice receiving different treatments, $n = 3$. C) Relative tumor volume curves of EcN-colonized tumors in mice after different treatments, $n = 4$. D) Survival fractions of mice after different treatments within 60 days. E) H&E- and Tunel- stained images of tumor tissues from all groups. **** $p < 0.0001$, *** $p < 0.001$, ** $p < 0.01$, * $p < 0.05$, ns $p > 0.05$, respectively.

prolonged to 58 days. In contrast, no mice died within 60 days after sNP@G/IR+L treatment, confirming the distinct efficacy of sNP@G/IR against EcN-colonized tumors (Figure 5D).

In addition, the tumor tissues from mice were stained with H&E and Tunel. The images exhibited that sNP@G/IR+L caused the most serious damage to the tumor tissues and induced the most severe cell apoptosis (Figure 5E). Biomarkers (including ALT, ALB, BUN, and CR) in serum from mice were further evaluated and no obvious difference was found compared with the PBS group, indicating the biosafety of above all treatments (Figure S26, Supporting Information). These results demonstrated that the biocompatible sNP@G/IR combined with chemotherapy and PTT showed the superior therapeutic efficacy on cancer by killing the tumor-resident bacteria.

2.7. Immune Evaluation on Bacteria-Colonized Tumor Model

The bacteria's death can accelerate the release of lipopolysaccharide (LPS) from gram-negative bacteria, which facilitates the maturation of dendritic cells (DCs).[11,30] Moreover, PTT can also activate the immune-response in tumor therapy.[31] Thus, we evaluated whether the multifunctional sNP@G/IR+L elicited the immune response in EcN-colonized Pan02 tumors. The rates of mature DCs and $CD8^+$ T cells in tumors and spleens were detected. The proportion of mature DCs collected from tumors of sNP@G-treated mice reached 29.70%, which was 2.72 times that from the free Gem treatment due to the dual antibacterial and anticancer effects (**, $p = 0.002$). Obviously, the proportion of mature DCs reached 47.30% in the sNP@G/IR+L group, which was 1.59 times that of the sNP@G group (***, $p = 0.0005$), confirming that the immune response was significantly enhanced (**Figure 6**A, and Figure S27, Supporting Information). Furthermore, the intratumor infiltration of $CD8^+$ T cells was tested to explore the DC-mediated immune response.[31] The percentages of $CD8^+$ T cells in tumor and spleen of control group were 7.72% and 19.26% respectively, while sNP@G/IR+L treatment increased the percentages to 32.72% (***, $p = 0.0002$) and 32.85% (****, $p = 0.00009$) respectively (Figure 6B,C and Figures S28 and S29, Supporting Information). Additionally, an immuno FL assay was used to check $CD8^+$ T cells in tumor tissues, which were labeled with red FL. The images displayed that $CD8^+$ T cells infiltrated tumor most in sNP@G/IR+L group (Figure 6D,E), and the red FL intensity was significantly stronger than that of PBS group (***, $p = 0.0007$). Proinflammatory cytokines (IL-10, IL-6, TNF-α, INF-γ) in serum were further

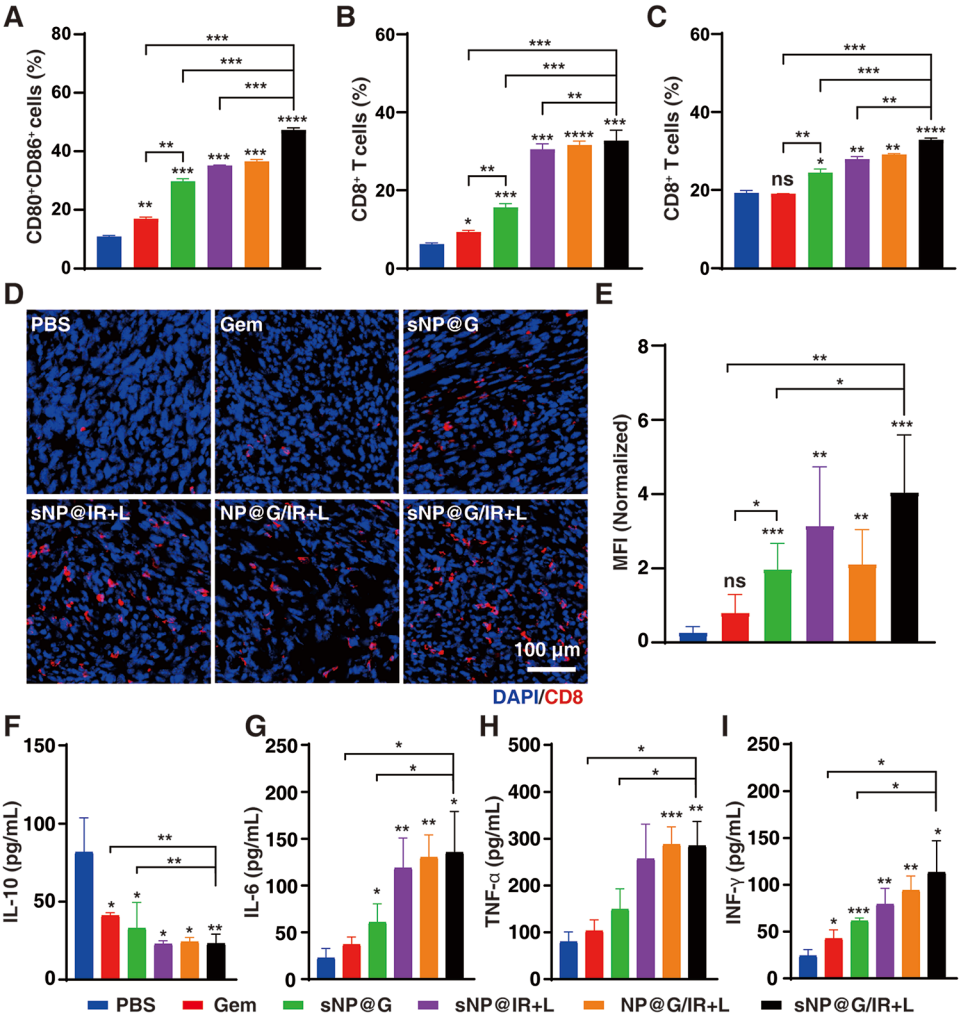

Figure 6. Immune activation by sNP@G/IR on a bacteria-colonized tumor model. A) Mature DCs in tumors, B) $CD8^+$ T cells in tumors, and C) $CD8^+$ T cells in spleens collected from bacteria-colonized Pan02-tumor-bearing mice after different treatments, $n = 3$. D) Images of $CD8^+$ T cell-immunofluorescence staining of tumor tissues from mice after different treatments. E) The corresponding mean FL intensity (MFI) analysis, $n = 5$. F) IL-10, G) IL-6, H) TNF-α, and I) INF-γ expression in the serum detected by ELISA kits, $n = 3$. **** $p < 0.0001$, *** $p < 0.001$, ** $p < 0.01$, * $p < 0.05$, and ns $p > 0.05$, respectively.

quantified through an enzyme-linked immunosorbent assay (ELISA). As shown in Figure 6F–I, sNP@G/IR+L treatment remarkably decreased the IL-10 (*, $p = 0.01$) level, but increased the IL-10 (*, $p = 0.01$), TNF-α (**, $p = 0.003$) and INF-γ (*, $p = 0.01$) levels. Taken together, the sNP@G/IR activated the tumor immune response, which reinforced anticancer capability.

3. Conclusion

This study proposed a dual-cascade responsive drug delivery system sNP@G/IR to enhance anticancer efficacy. This sNP@G/IR offered a new case of non-antibiotic therapy, displaying optimal antibacterial activity and selectivity with precise modulating of the guanidine units. The design of dual-cascade responsive endowed sNP@G/IR with multiple functional advantages, including active tumor targeting, deep tumor penetration, increased cellular internalization, and controlled drug release. By eliminating tumor-resident intracellular bacteria and augmenting drug delivery efficacy, sNP@G/IR overcame bacteria-mediated Gem inactivation, greatly suppressed bacteria-colonized tumors as well as activated tumor immunity. Overall, this study provides a promising "offensive-defensive" strategy to enhance cancer therapy.

Supporting Information

Supporting Information is available from the Wiley Online Library or from the author.

Acknowledgements

The authors thank the National Natural Science Foundation (21574008, 52003161), the National Mega-project for Innovative Drugs (2019ZX09721001-007-002), and the Fundamental Research Funds

for the Central Universities (BHYC1705B) of China for the financial support. All animals were treated and cared for in accordance with the National Research Council's Guide for the care and use of laboratory animals and under the supervision and assessment by the SPF Animal Department of Clinical Institute in China-Japan Friendship Hospital (Approval no.: zryhyy 12-20-08-3). X.W. acknowledges Prof. Lizeng Gao from the Institute of Biophysics Chinese Academy of Sciences for gifting the model bacteria (*E. coli* Nissle 1917 and GFP labeled *E. coli* Nissle 1917). X.W. acknowledges Associate Prof. Zhao Yang from Beijing University of Chemical Technology for the help of the intracellular bacteria test.

Conflict of Interest

The authors declare no conflict of interest.

Authors Contribution

X.W. conceived the project. X.K. and X.W. designed the experiments. X.K. performed experimental work and analyzed the data with the help of F.B., W.F., G.L., H.X., and X.W. In vivo assessments were performed with the help of F.B., W.F., F.L., X.Y., H.L., and Y.Y. The manuscript was drafted by X.K. The manuscript was edited by Y.Y., G.L., H.X., and X.W. All authors discussed the results and commented on the manuscript.

Data Availability Statement

Research data are not shared.

Keywords

bacteria-mediated drug inactivation, dual-cascade responsive nanoparticles, pancreatic cancer, precise drug delivery, tumor-resident intracellular bacteria

Received: July 25, 2022
Published online:

[1] a) J. D. Mizrahi, R. Surana, J. W. Valle, R. T. Shroff, *Lancet* **2020**, *395*, 2008; b) E. Riquelme, Y. Zhang, L. Zhang, M. Montiel, M. Zoltan, W. Dong, P. Quesada, I. Sahin, V. Chandra, A. San Lucas, P. Scheet, H. Xu, S. M. Hanash, L. Feng, J. K. Burks, K. A. Do, C. B. Peterson, D. Nejman, C. D. Tzeng, M. P. Kim, C. L. Sears, N. Ajami, J. Petrosino, L. D. Wood, A. Maitra, R. Straussman, M. Katz, J. R. White, R. Jenq, J. Wargo, et al., *Cell* **2019**, *178*, 795; c) T. Murakami, Y. Hiroshima, R. Matsuyama, Y. Homma, R. M. Hoffman, I. Endo, *Ann. Gastroenterol. Surg.* **2019**, *3*, 130.

[2] a) P. P. Adiseshaiah, R. M. Crist, S. S. Hook, S. E. McNeil, *Nat. Rev. Clin. Oncol.* **2016**, *13*, 750; b) Q. Zhou, S. Shao, J. Wang, C. Xu, J. Xiang, Y. Piao, Z. Zhou, Q. Yu, J. Tang, X. Liu, Z. Gan, R. Mo, Z. Gu, Y. Shen, *Nat. Nanotechnol.* **2019**, *14*, 799.

[3] M. Amrutkar, I. P. Gladhaug, *Cancers* **2017**, *9*, 157.

[4] a) M. J. Mitchell, M. M. Billingsley, R. M. Haley, M. E. Wechsler, N. A. Peppas, R. Langer, *Nat. Rev. Drug Discovery* **2021**, *20*, 101; b) Y. Wang, Z. Zhang, C. Zheng, X. Zhao, Y. Zheng, Q. Liu, Y. Liu, L. Shi, *Small* **2021**, *17*, e2100578.

[5] a) Z. Zhang, H. Wang, T. Tan, J. Li, Z. Wang, Y. Li, *Adv. Funct. Mater.* **2018**, *28*, 40; b) X. Pan, P. Li, L. Bai, J. Ma, S. Li, F. Zhang, S. Liu, Q. Wu, H. Shen, H. Liu, *Small* **2020**, *16*, 2000809; c) Y. He, L. Lei, J. Cao, X. Yang, S. Cai, F. Tong, D. Huang, H. Mei, K. Luo, H. Gao, B. He, N. A. Peppas, *Sci. Adv.* **2021**, *7*, eaba0776; d) J. Chen, J. Ding, Y. Wang, J. Cheng, S. Ji, X. Zhuang, X. Chen, *Adv. Mater.* **2017**, *29*, 1701170; e) H. Han, Y. Hou, X. Chen, P. Zhang, M. Kang, Q. Jin, J. Ji, M. Gao, *J. Am. Chem. Soc.* **2020**, *142*, 4944; f) Q. Sun, Y. Zhu, J. Du, *Biomed. Mater.* **2021**, *16*, 042010.

[6] a) X. He, X. Chen, L. Liu, Y. Zhang, Y. Lu, Y. Zhang, Q. Chen, C. Ruan, Q. Guo, C. Li, T. Sun, C. Jiang, *Adv. Sci.* **2018**, *5*, 1701070; b) Y. Wang, D. Huang, X. Wang, F. Yang, H. Shen, D. Wu, *Biomater. Sci.* **2019**, *7*, 3238; c) J. Liu, C. Chen, T. Wei, O. Gayet, C. Loncle, L. Borge, N. Dusetti, X. Ma, D. Marson, E. Laurini, S. Pricl, Z. Gu, J. Iovanna, L. Peng, X. Liang, *Exploration* **2021**, *1*, 21; d) S. Zhang, S. Zhou, H. Liu, M. Xing, B. Ding, B. Li, *Adv. Funct. Mater.* **2020**, *30*, 2002434.

[7] a) G. Housman, S. Byler, S. Heerboth, K. Lapinska, M. Longacre, N. Snyder, S. Sarkar, *Cancers* **2014**, *6*, 1769; b) B. Mansoori, A. Mohammadi, S. Davudian, S. Shirjang, B. Baradaran, *Adv. Pharm. Bull.* **2017**, *7*, 339; c) H. Zahreddine, K. L. Borden, *Front. Pharmacol.* **2013**, *4*, 28.

[8] L. T. Geller, M. Barzily-Rokni, T. Danino, O. H. Jonas, N. Shental, D. Nejman, N. Gavert, Y. Zwang, Z. A. Cooper, K. Shee, C. A. Thaiss, A. Reuben, J. Livny, R. Avraham, D. T. Frederick, M. Ligorio, K. Chatman, S. E. Johnston, C. M. Mosher, A. Brandis, G. Fuks, C. Gurbatri, V. Gopalakrishnan, M. Kim, M. W. Hurd, M. Katz, J. Fleming, A. Maitra, D. A. Smith, M. Skalak, et al., *Science* **2017**, *357*, 1156.

[9] C. Jobin, *Nature* **2017**, *550*, 337;

[10] X. Zhang, X. Chen, Y. Guo, G. Gao, D. Wang, Y. Wu, J. Liu, G. Liang, Y. Zhao, F. G. Wu, *Angew. Chem., Int. Ed.* **2021**, *60*, 14013.

[11] a) D. Nejman, I. Livyatan, G. Fuks, N. Gavert, Y. Zwang, L. T. Geller, A. Rotter-Maskowitz, R. Weiser, G. Mallel, E. Gigi, A. Meltser, G. M. Douglas, I. Kamer, V. Gopalakrishnan, T. Dadosh, S. Levin-Zaidman, S. Avnet, T. Atlan, Z. A. Cooper, R. Arora, A. P. Cogdill, M. A. W. Khan, G. Ologun, Y. Bussi, A. Weinberger, M. Lotan-Pompan, O. Golani, G. Perry, M. Rokah, K. Bahar-Shany, et al., *Science* **2020**, *368*, 973. b) A. Fu, B. Yao, T. Dong, Y. Chen, J. Yao, Y. Liu, H. Li, H. Bai, X. Liu, Y. Zhang, C. Wang, Y. Guo, N. Li, S. Cai, *Cell* **2022**, *185*, 1356.

[12] W. Feng, G. Li, X. Kang, R. Wang, F. Liu, D. Zhao, H. Li, F. Bu, Y. Yu, T. F. Moriarty, X. Wang, *Adv. Mater.* **2022**, *34*, 2109789.

[13] P. P. Kalelkar, M. Riddick, A. J. García, *Nat. Rev. Mater.* **2021**, *7*, 39.

[14] a) M. Zhou, Y. X. Qian, J. Y. Xie, W. J. Zhang, W. N. Jiang, X. M. Xiao, S. Chen, C. Z. Dai, Z. H. Cong, Z. M. Ji, N. Shao, L. Q. Liu, Y. Q. Wu, R. H. Liu, *Angew. Chem., Int. Ed.* **2020**, *59*, 6412; b) X. Ding, C. Yang, W. Moreira, P. Y. Yuan, B. Periaswamy, P. F. de Sessions, H. M. Zhao, J. R. Tan, A. Lee, K. X. Ong, N. Park, Z. C. Liang, J. L. Hedrick, Y. Y. Yang, *Adv. Sci.* **2020**, *7*, 2001374. c) J. Sun, M. Li, M. Lin, B. Zhang, X. Chen, *Adv. Mater.* **2021**, *33*, 2104402.

[15] Y. Wang, Y. Jiang, D. Wei, P. Singh, Y. Yu, T. Lee, L. Zhang, H. K. Mandl, A. S. Piotrowski-Daspit, X. Chen, F. Li, X. Li, Y. Cheng, A. Josowitz, F. Yang, Y. Zhao, F. Wang, Z. Zhao, A. Huttner, R. S. Bindra, H. Xiao, W. M. Saltzman, *Nat. Biomed. Eng.* **2021**, *5*, 1048.

[16] a) M. Ye, Y. Zhao, Y. Wang, M. Zhao, N. Yodsanit, R. Xie, D. Andes, S. Gong, *Adv. Mater.* **2021**, *33*, 2006772; b) H. Han, J. Zhu, D. Q. Wu, F. X. Li, X. L. Wang, J. Y. Yu, X. H. Qin, *Adv. Funct. Mater.* **2019**, *29*, 1806594.

[17] a) F. Wu, J. Xu, R. Yan, B. Hu, G. Li, M. Jin, X. Jiang, J. Li, P. Tang, J. Zhu, *Biomed. Mater.* **2020**, *15*, 045016; b) R. Wu, M. Song, D. Sui, S. Duan, F.-J. Xu, *J. Mater. Chem. B* **2022**, *10*, 2471.

[18] A. Chen, A. Karanastasis, K. R. Casey, M. Necelis, B. R. Carone, G. A. Caputo, E. F. Palermo, *ACS Appl. Mater. Interfaces* **2020**, *12*, 21270.

[19] Y. Wu, W. Jiang, Z. Cong, K. Chen, Y. She, C. Zhong, W. Zhang, M. Chen, M. Zhou, N. Shao, *J. Med. Chem.* **2022**, *65*, 7296.
[20] a) A. C. Hortelão, T. Patiño, A. Perez-Jiménez, À. Blanco, S. Sánchez, *Adv. Funct. Mater.* **2018**, *28*, 1705086; b) Y. K. Sung, S. W. Kim, *Biomater. Res.* **2020**, *24*, 12.
[21] a) Y. Guo, Y. Xu, Q. Bao, C. Shen, D. Ni, P. Hu, J. Shi, *ACS Nano* **2021**, *15*, 16286; b) D. Yang, W. Chen, J. Hu, *J. Phys. Chem. B* **2014**, *118*, 12311.
[22] A. Tsiasioti, I. Iakovidou, C. K. Zacharis, P. D. Tzanavaras, *Spectrochim. Acta, Part A* **2020**, *229*, 117963.
[23] X. Meng, J. Zhang, Z. Sun, L. Zhou, G. Deng, S. Li, W. Li, P. Gong, L. Cai, *Theranostics* **2018**, *8*, 6025.
[24] K. Zhang, Y. Du, Z. Si, Y. Liu, M. E. Turvey, C. Raju, D. Keogh, L. Ruan, S. L. Jothy, S. Reghu, K. Marimuthu, P. P. De, O. T. Ng, J. R. Mediavilla, B. N. Kreiswirth, Y. R. Chi, J. Ren, K. C. Tam, X. W. Liu, H. Duan, Y. Zhu, Y. Mu, P. T. Hammond, G. C. Bazan, K. Pethe, M. B. Chan-Park, *Nat. Commun.* **2019**, *10*, 4792.
[25] X. Li, H. Bai, Y. Yang, J. Yoon, S. Wang, X. Zhang, *Adv. Mater.* **2019**, *31*, 1805092.
[26] a) M. Li, J. Sun, W. Zhang, Y. Zhao, S. Zhang, S. Zhang, *Carbohydr. Polym.* **2021**, *251*, 117103; b) X. Kang, Y. Wang, Z. Chen, Y. Wu, H. Chen, X. Yang, C. Yu, *Chem. Commun.* **2020**, *56*, 11271; c) X. Kang, Y. Yu, Z. Chen, Y. Wu, D. Wei, Y. Zhao, F. Wang, H. Xiao, *J. Mater. Chem. B* **2019**, *7*, 3346.
[27] a) F. Sun, Q. Zhu, T. Li, M. Saeed, Z. Xu, F. Zhong, R. Song, M. Huai, M. Zheng, C. Xie, L. Xu, H. Yu, *Adv. Sci.* **2021**, *8*, 2002746; b) Q. Zhang, G. Kuang, S. He, H. Lu, Y. Cheng, D. Zhou, Y. Huang, *Nano Lett.* **2020**, *20*, 3039; c) K. Y. Choi, H. S. Han, E. S. Lee, J. M. Shin, B. D. Almquist, D. S. Lee, J. H. Park, *Adv. Mater.* **2019**, *31*, 1803549.
[28] a) F. Wang, W. Sun, L. Li, L. Li, Y. Liu, Z. R. Zhang, Y. Huang, *ACS Appl. Mater. Interfaces* **2017**, *9*, 27563; b) J. Ma, P. Li, W. Wang, S. Wang, X. Pan, F. Zhang, S. Li, S. Liu, H. Wang, G. Gao, B. Xu, Q. Yuan, H. Shen, H. Liu, *ACS Nano* **2018**, *12*, 9022.
[29] J. Stritzker, S. Weibel, P. J. Hill, T. A. Oelschlaeger, W. Goebel, A. A. Szalay, *Int. J. Med. Microbiol.* **2007**, *297*, 151.
[30] a) X. Huang, J. Pan, F. Xu, B. Shao, Y. Wang, X. Guo, S. Zhou, *Adv. Sci.* **2021**, *8*, 2003572; b) W. Song, K. Tiruthani, Y. Wang, L. Shen, M. Hu, O. Dorosheva, K. Qiu, K. A. Kinghorn, R. Liu, L. Huang, *Adv. Mater.* **2018**, *30*, 1805007.
[31] a) M. Chang, Z. Hou, M. Wang, C. Li, J. Lin, *Adv. Mater.* **2021**, *33*, 2004788; b) Y. Jiang, J. Huang, C. Xu, K. Pu, *Nat. Commun.* **2021**, *12*, 742.